ORIGINAL PAPER

J. M. Catalán ⬡ · M. Moriche ⬡ · O. Flores ⬡ ·
M. García-Villalba ⬡

On the settling of a spherical particle in slightly perturbed ambient fluid

Abstract Direct numerical simulations of the settling of a spherical particle under the action of gravity in a slightly perturbed ambient fluid have been performed. The ambient perturbations are generated using a synthetic turbulence inflow generator method, and their length scale and intensity are varied to study their influence on the particle motion. The Galileo number is 151 and the solid-to-fluid density ratio is 1.5, so that in the absence of perturbations, the particle settles following a steady vertical trajectory. It has been found that the ambient perturbations trigger the formation of double-threaded vortical structures in the wake of the particle. These structures resemble those that appear in the oblique oscillating regime that is found in the absence of perturbations at higher Galileo numbers. Due to the flow perturbations the particle is pushed randomly in all directions, and this results in a combination of slow lateral drifts along fixed directions and relatively fast excursions in random directions. The particle response has been characterized using probability density functions of the velocity in the cross-plane and persistence probability. The slow drifts are strongly influenced by the size of the perturbations and by the rotational motion of the particle, while the intensity of the perturbations seems to play a minor role.

1 Introduction

In recent years, considerable attention has been devoted to studying particle-laden flows, given their importance in a large variety of fields, such as biological flows, sediment transport, fluidized beds, and volcanic eruptions [2,4,35]. These flows usually exhibit a great variety of dynamical features. For relatively large particles and in the presence of gravity, the flows are typically turbulent, and the fluid–particle interactions are strongly coupled: the turbulence modifies the particle trajectories and the motion of the particles modifies the characteristics of the surrounding turbulence. Even in the absence of turbulence, the resulting flows are still very complicated. For example, for dilute systems of settling particles in quiescent fluid, different types of particle arrangements have been observed. At low Reynolds number, Re $\leq$ 10, dilute suspensions of spherical particles tend to align horizontally in pairs [43]. At higher Reynolds number, large-scale columnar clusters have been observed to appear, both for spherical and non-spherical particles [11,13,26,39]. When clusters form, the settling velocity of the particles increases and pseudo-turbulence is generated in the flow. Even when clusters are not formed, as

J. M. Catalán · O. Flores
Department of Aerospace Engineering, Universidad Carlos III de Madrid, Madrid, Spain

M. Moriche · M. García-Villalba (✉)
Institute of Fluid Mechanics and Heat Transfer, TU Wien, Vienna, Austria
E-mail: manuel.garcia-villalba@tuwien.ac.at

occurs for spheres at moderate Galileo numbers [39], their motion is influenced by flow perturbations generated by the surrounding, distant, settling spheres.

In view of these complications, researchers have often resorted to simpler configurations to understand basic mechanisms. For example, the relation between the flow in the wake and the hydrodynamic forces has been explored considering a fixed sphere in a uniform flow [27,37]. Such studies provided a first characterization of the different flow regimes that exist as a function of the particle Reynolds number. When the particle is released and settles under the action of gravity in unbounded, quiescent fluid, it has been found that path instabilities may arise due to the coupled solid–fluid motion [10]. For spherical particles, the problem is governed by two non-dimensional parameters [16], one being the density ratio between the particle and the fluid, ϱ, and the other the Galileo number,

$$\mathrm{Ga} = \frac{U_{\mathrm{g}} D}{\nu}, \tag{1}$$

where D is the particle diameter, ν is the kinematic viscosity of the fluid and $U_{\mathrm{g}} = \sqrt{|\varrho - 1| g D}$ is a gravitational velocity scale, g being the magnitude of the gravitational acceleration. Depending on these two parameters, a variety of particle path regimes have been encountered both numerically [44] and experimentally [7,12]. For the density ratio considered in the present study, ϱ slightly above 1, the particle settles on a steady vertical path until Ga $\approx$ 155. With increasing Ga, the particle settles on a steady oblique path. This is followed by unsteady path regimes. First, periodically in an oscillating oblique way and, finally, for Ga $\gtrsim$ 210, the settling trajectory becomes chaotic [16].

Much less is known about the particle response when the ambient flow is slightly perturbed. Mittal [22] studied the response of a fixed sphere subject to a free stream with sinusoidal perturbations. He found that even at low Reynolds numbers, where the wake is not susceptible to natural vortex shedding, free-stream fluctuations can induce flapping and breakup of the separated shear layers, inducing large perturbations in the near wake. In the present study, we aim to extend the work of Mittal [22] to explore the dynamic response of a free particle that settles under the action of gravity in an ambient flow with isotropic velocity perturbations. As in previous studies [25,40], we will perform direct numerical simulations using a computational domain that moves with the mean settling velocity of the particle in an inflow–outflow configuration. These simulations require injecting ambient velocity perturbations upstream of the particle, which increases the difficulty of these already challenging simulations.

The generation of turbulent or perturbed flow in numerical simulations is a topic that has been studied for many years. The problem is not trivial, since these perturbations need to be reasonably compatible with the flow equations (namely, the Navier–Stokes equations of the incompressible flow). Otherwise, the injected fluctuations are quickly damped by viscous and pressure forces. Early works on this topic are those of Juneja et al. [17] and Lund et al. [21]. The latter proposed a method to generate three-dimensional, time-dependent turbulent inflow data for simulations of spatially developing boundary layers, by using auxiliary simulations. Other authors developed methodologies to generate synthetic inflow turbulence as a superposition of coherent structures [15,29,30]. Many aspects of these methods have been recently discussed in a review by Wu [41].

In an influential work, Klein et al. [20] introduced a digital filter approach for generating inflow data for spatially developing simulations, avoiding the need of using auxiliary simulations. This was followed by a large amount of studies that made use of the digital filter approach [3,9,18,33,42]. Furthermore, Kempf et al. [19] proposed a modification of the method by Klein et al. [20] that led to a higher efficiency in terms of computational effort. Combining the ideas of Klein et al. [20] and Kempf et al. [19], a new methodology was presented by Schmidt and Breuer [34]. They proposed to introduce the flow perturbations in the vicinity of the region of interest, instead of at the inflow plane, by adding a source term to the Navier–Stokes equations. The advantage is that, often, coarse grids are used in the inflow region, and fluctuations introduced at the inlet usually decay before arriving at the region of interest. The benefits of this approach were demonstrated by Breuer [6], who studied the effect of free-stream turbulence on the flow over an airfoil with a laminar separation bubble. The method developed by Schmidt and Breuer [34] has been recently compared with grid-induced turbulence by Catalán et al. [8] showing that the former requires a shorter development region and results in a more isotropic velocity field than the latter. Consequently, in the present study, we will use the synthetic turbulence method developed by Schmidt and Breuer [34] to introduce the ambient velocity perturbations in our simulations.

The manuscript is organized as follows: In Sect. 2, the physical problem and the non-dimensional parameters controlling it are described. In Sect. 3, we present the methodology, including the numerical method and computational setup (Sect. 3.1), the generation of free-stream fluctuations (Sect. 3.2) and the definition of

persistence (Sect. 3.3) , which is the probability of the particle to keep moving along a roughly fixed direction. In Sect. 4, we show and analyze the results of our study using flow visualizations and time signals of particle position and particle velocity. The paper closes with a summary and discussion in Sect. 5.

2 Problem description

We analyze the gravitational settling of a spherical particle of diameter D and uniform density ρ_p in a perturbed ambient flow. The fluid is assumed to be Newtonian with constant density ρ_f and kinematic viscosity ν. The fluid velocity, $\mathbf{u} = (u_x, u_y, u_z)$, and pressure, p, are governed by the Navier–Stokes equations of an incompressible flow

$$\nabla \cdot \mathbf{u} = 0 \,, \tag{2a}$$

$$\frac{\partial \mathbf{u}}{\partial t} + (\mathbf{u} \cdot \nabla)\mathbf{u} = -\frac{1}{\rho_f}\nabla p + \nu \nabla^2 \mathbf{u} \,. \tag{2b}$$

The velocity of the center of gravity of the particle, $\mathbf{u}_p = (u_{px}, u_{py}, u_{pz})$, and the angular velocity, $\mathbf{\Omega}$, are governed by the Newton–Euler equations

$$V_p \rho_p \frac{d\mathbf{u}_p}{dt} = \mathbf{F}_H + V_p(\rho_p - \rho_f)\mathbf{g} \,, \tag{3a}$$

$$I_G \frac{d\mathbf{\Omega}}{dt} = \mathbf{M}_H \,, \tag{3b}$$

where V_p is the volume of the particle, I_G is the moment of inertia with respect to an axis passing through the center of gravity, $\mathbf{g}$ is the gravitational acceleration, $\mathbf{F}_H$ is the hydrodynamic force and $\mathbf{M}_H$ is the hydrodynamic torque with respect to the center of gravity.

In the absence of flow perturbations, the problem is governed by the density ratio between the particle and the fluid, $\varrho = \rho_p/\rho_f$, and the Galileo number [see Eq. (1)]. Independently of the density ratio ϱ, the first bifurcation of the flow regime occurs at Ga $\simeq$ 155 [16]. In the present study, we have set $\varrho = 1.5$ and a nominal Ga = 151, so that in the absence of perturbations the sphere settles on a steady vertical path. We aim to study how small, isotropic perturbations in the ambient flow affect the settling of the particle (see Fig. 1a). By selecting Ga close to the value of the first bifurcation, we want to explore if any of the subsequent flow regimes (steady oblique, oscillating oblique, etc) are triggered by the perturbations in the ambient fluid.

In order to characterize the size and intensity of the perturbations, we use the integral length scale, Λ, and the root mean square of the velocity fluctuations, u'. This results in a total of four governing parameters, namely Ga, ϱ, Λ/D and u'/U_g. Regarding the flow perturbations, we are interested in fluctuations able to trigger any of the flow regimes that follow after the steady vertical path of a sphere settling in quiescent fluid. To that end,
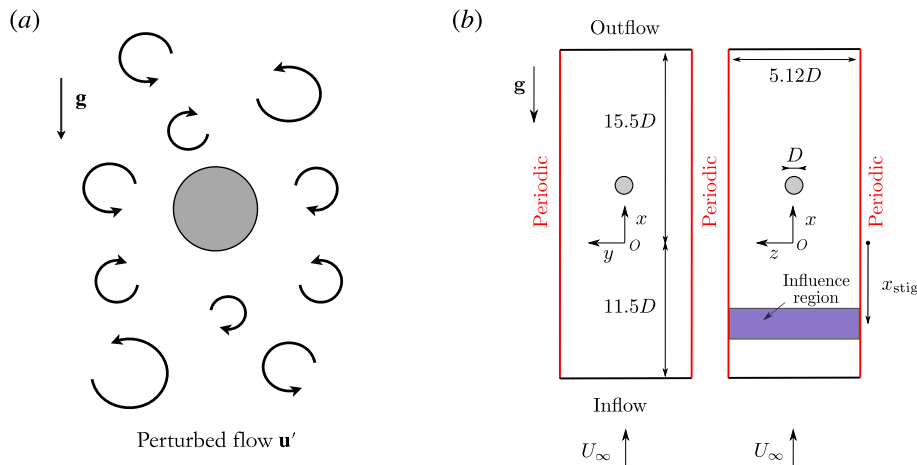

Fig. 1 **a** Sketch of the problem. **b** Computational domain indicating boundary conditions, STIG influence region and location of the Eulerian reference frame

Table 1 Simulation parameters

Case	x_{stig}/D	Λ/D	u'/U_{g} (%)	Re_s
1	-4	1.137	1.23	186.51
2	-4	1.137	3.70	186.52
3	-6.5	2.274	1.23	186.79
4	-6.5	2.274	3.70	186.87

we consider fluctuations whose integral length scale is: $\Lambda/D = 2.274$ to roughly match the frequency of the oblique oscillating regime ($f \simeq 0.07 U_{\text{g}}/D$, as reported by Uhlmann and Dušek [40]), and $\Lambda/D = 1.137$ to provide a case with twice that frequency with exploratory purposes. Based on preliminary simulations in which we observed an influence on the solution with low-intensity perturbations, we select for this study $u'/U_s = 1\%$ and 3%, where U_s is the mean settling velocity. This results in four nominal cases, labeled 1 to 4, as shown in Table 1 (please note that in terms of U_{g}, the selected intensities result in $u'/U_{\text{g}} = 1.23\%,\ 3.7\%$). Additionally, we analyze in Sect. 4.4 two cases in which we have removed the vertical translation of the particle (cases 1.2 and 2.2), and one in which we suppress its angular motion (case 1.3), to evaluate the effect of particle mobility on the resultant flow regimes.

Finally, it is important to note that even if the perturbations introduced in the flow are random in nature, they do not correspond to a turbulent flow. The Reynolds number $\text{Re}_\Lambda = \Lambda u'/\nu$ varies in the range 2–13 for the cases presented here, where Λ is the integral length scale and u' is the root mean square of the velocity fluctuations. The low values of Re_Λ indicate that the perturbations are not multi-scale in nature, so that there is no effective separation between energy containing scales (i.e., Λ, which is comparable to D) and dissipative scales. Consequently, the cases reported herein can be considered intermediate between particles settling in a quiescent ambient (i.e., laminar regime) and particles settling in a turbulent flow.

In order to frame better our study with respect to the latter regime, here we provide some non-dimensional numbers typically used for particles settling in turbulent flows. The Rouse number is $\text{Ro} = U_s/u' = 100$ for cases 1 and 3, and $\text{Ro} = 33$ for cases 2 and 4. The ratio of particle diameter to integral scale is $D/\Lambda = 0.88$ for cases 1 and 2, and $D/\Lambda = 0.44$ for cases 3 and 4. The Stokes number $S_t = \tau_{\text{p}}/\tau_{f,\Lambda}$, based on the characteristic time of the fluctuations $\tau_{f,\Lambda} = \Lambda/u'$ and the response time of a particle $\tau_{\text{p}} = (4\varrho D)/(3U_s C_x)$ (where C_x is the mean drag obtained in the simulations presented below, which is similar to the correlation of [32]), is $S_t = \mathcal{O}(10^{-2})$ for all cases. As a consequence, the particle motion should be influenced by the flow perturbations. This should be true at least for the lateral motion. The vertical motion is probably governed by the Stokes number based on the gravitational velocity which is significantly larger.

3 Methodology

3.1 Numerical method and computational setup

The simulations presented in this work have been performed using TUCAN [23,24], an in-house code that solves the Navier–Stokes equations for an incompressible flow, using a fractional step method on a uniform staggered Cartesian grid. The time integration is performed by means of a semi-implicit low-storage three-stage Runge–Kutta method, and the spatial derivatives are discretized with centered, second-order finite differences. The presence of the body as well as the coupling with the fluid equations are accounted for using the direct forcing immersed boundary method originally proposed by Uhlmann [38], as discussed in Arranz et al. [1].

The size of the computational domain is $27D \times 5.12D \times 5.12D$ in the x, y and z directions, where x is the vertical direction (see Fig. 1b), and the spatial resolution is $D/\Delta x = 25$. For convenience, we set the origin of the domain O ($x = 0$), at a distance of $11.5D$ from the bottom boundary (see Fig. 1b). This results in a computational domain similar to that of Uhlmann and Dušek [40], but enlarged in the vertical direction to accommodate possible particle drifts due to long integration times. The particle is initially located at the origin ($x = 0$), except for the cases with more intense perturbations, which are restarted from a converged case with lower intensity fluctuations. The time step, Δt, is selected such that the maximum CFL is approximately 0.3, meaning that fluid particles travel a maximum distance of around $0.3\Delta x$ at each time step Δt, ensuring stability. We compute this number at each grid point (i, j, k) as

$$\text{CFL}_{ijk} = \frac{(|u_x| + |u_y| + |u_z|)_{ijk}\, \Delta t}{\Delta x}. \tag{4}$$

We impose a uniform free stream of velocity U_∞ at the bottom boundary, an advective boundary condition at the top boundary and periodicity in the lateral directions.

Please note that U_∞ is the mean settling velocity of the particle if the time-averaged, vertical position of the particle remains constant during the course of the simulation. We conduct the simulations trying to achieve this goal, and in order to do so, we proceed as in [40]. These authors perform a simulation with the particle fixed to estimate the drag on the particle. This information is then used to adjust the value of g. Following this procedure, the value of Ga does not exactly correspond to the nominal one (with a variation below 0.7% for all cases in the present study). Furthermore, for very long time intervals, it is also not possible to avoid small drifts. In the present study, we have observed vertical drifts smaller than $1D$ for time intervals of $\mathcal{O}(10^3 D/U_g)$. Due to the small vertical drifts, the actual mean settling velocity of the particle, U_s, differs slightly from U_∞. Therefore, we define the particle Reynolds number as $\mathrm{Re}_s = U_s D/\nu$; the values are reported in Table 1.

3.2 Generation of free-stream fluctuations

Following the work of Schmidt and Breuer [34], we use the Synthetic Turbulence Inflow Generator (STIG) method to produce the free-stream perturbations encountered by the settling particle. The method requires introducing an additional volume force in the fluid momentum equation (2b)

$$\mathbf{f}_{\text{stig}}(x, y, z, t) = \begin{cases} \dfrac{\mathbf{u}'_{\text{f}}(t,y,z)}{T} \exp\left(-\dfrac{\pi}{2}\dfrac{(x - x_{\text{stig}})^2}{\Lambda^2}\right), & \text{if} \quad -n_\Lambda \Lambda \leq (x - x_{\text{stig}}) \leq n_\Lambda \Lambda, \\ 0, & \text{otherwise,} \end{cases} \tag{5}$$

where $\mathbf{u}'_{\text{f}}$ is a fluctuation velocity, T is the time scale of the perturbations, x_{stig} represents the location at which the perturbations are injected, and n_Λ is a factor used to limit the extent of the injection region (otherwise infinite) that we set to $n_\Lambda = 2$. Details of how to generate the perturbation velocity field $\mathbf{u}'_{\text{f}}$ can be found in "Appendix A" and in the work of [34]. The perturbation time scale T is related to the integral length scale Λ through Taylor's hypothesis [36]; therefore, $T = \Lambda/U_\infty$ is not an additional parameter of our problem. We select $x_{\text{stig}} = -4D$ and $-6.5D$ for the cases with integral length scale $\Lambda/D = 1.137$ and 2.274, respectively, to account for the different length of the injection region, which depends on Λ as it can be seen in Eq. (5). The region of influence of the injected perturbations extends over the whole (y, z) plane of the computational domain because the particle is free to move. A sketch can be found in Fig. 1b. Using the source term method, the intensity of the fluctuations is enforced indirectly in the region of influence. The intensity that the particle experiences is somewhat lower since the fluctuations decay along the streamwise direction. This effect is characterized in Table 3 in "Appendix A".

3.3 Persistence

In order to characterize the trends of the horizontal particle motion, we employ the concept of persistence, in a similar fashion as other authors [5,31]. We define the persistence, $P(T_\theta, \gamma)$, as the probability of a particle to keep moving along the same direction in the cross-plane (within some tolerance γ) over a period of time T_θ. In order to compute P, we first compile time series of $\theta(t) = \arctan(u_{pz}/u_{py})$, which is the angle formed by the cross-plane particle velocity components, u_{py} and u_{pz}. We then define a series of intervals (i.e., $t \in [t_i^*, t_i^* + T_\theta]$) of equal duration T_θ, which are allowed to overlap. For each interval we define a binary variable

$$\mathrm{IP}_i(T_\theta, \gamma) = \begin{cases} 1 & \text{if} \quad \max\left(\left|\theta(t_i^* + t) - \langle\theta(t)\rangle\right|\right) < \gamma \quad, \quad t \in [t_i^*, t_i^* + T_\theta], \\ 0 & \text{otherwise,} \end{cases} \tag{6}$$

where γ is the chosen tolerance and the averaging operator $\langle\cdot\rangle$ is computed over the i-th interval. Having computed $\mathrm{IP}_i(T_\theta, \gamma)$ for all available intervals, we compute the persistence as

$$P(T_\theta, \gamma) = \frac{1}{N}\sum_{i=1}^{N} \mathrm{IP}_i(T_\theta, \gamma), \tag{7}$$

where N is the number of available intervals. For the sake of obtaining better statistics, and considering the discrete nature of our results, we define our intervals with the maximum possible overlap, resulting in $t_i^* = t_{i-1}^* + \Delta t$.

4 Results

In this section, we present the results of the cases described in Table 1. All the cases have been integrated for at least $1100D/U_g$, and we have selected the last available interval of $1000D/U_g$ to compute statistics. This results in a discarded transient of more than $100D/U_g$, corresponding to about 4 flow-through times. This is more than sufficient time for the perturbations to fill the entire domain and for the solution to remove its dependence with the initialization procedure (see Fig. 4). Note that the time interval employed for the statistical characterization is very long when compared to the characteristic time of the flow perturbations, T, which is of $O(1)D/U_g$. The reason for this (as will be shown below) is that long drifts are observed in the time evolution of the particle position, and their statistical characterization requires very long integration times. Three additional simulations that consider restrictions of either the rotation or the vertical translation of the particle are also discussed below.

4.1 Flow visualization

We start by providing a visual impression of the flow differences between the cases. This is done by using a 3D visualization in Fig. 2 and a 2D visualization in a vertical plane that passes through the particle center in Fig. 3. The 3D visualizations are complemented in the Supplementary Material by the corresponding animations. Figure 2 shows isosurfaces of the second invariant of the velocity gradient tensor, Q, Hunt et al. [14] colored
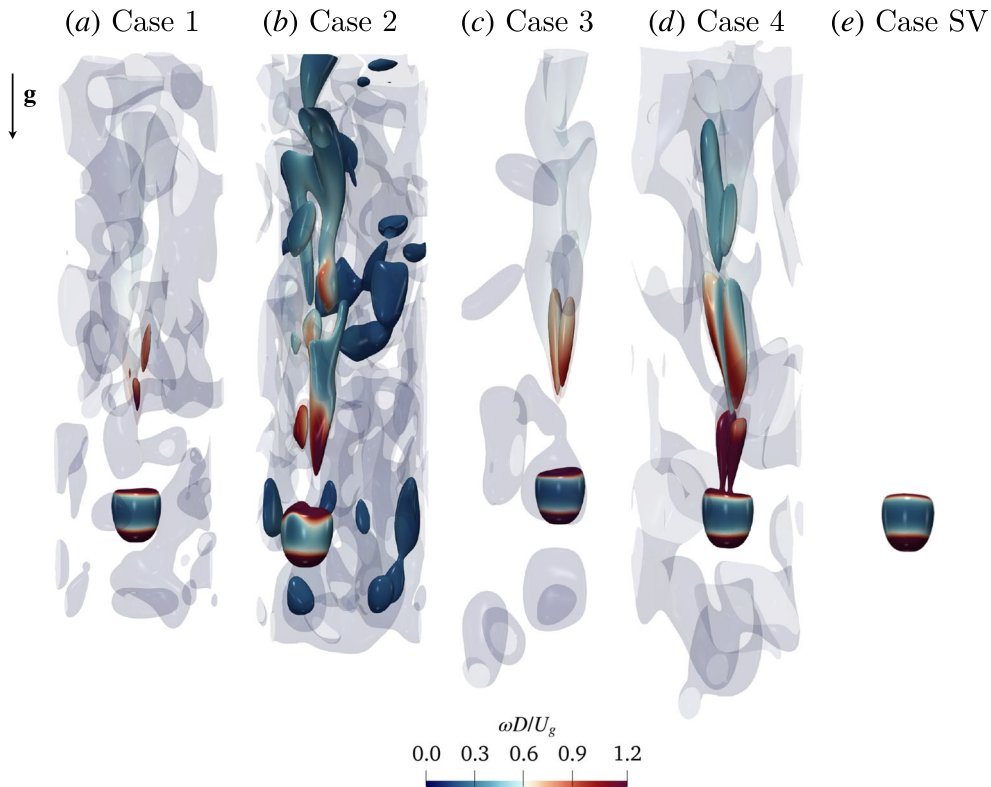

Fig. 2 Instantaneous vortical structures for the nominal cases (1, 2, 3 and 4) and for the steady vertical case (SV, without velocity perturbations). The isosurfaces correspond to values of the non-dimensional Q-criterion, $QD^2/U_g^2 = [0.006,\ 0.00012]$, colored by the magnitude of the vorticity ω. The isosurfaces with lower threshold of Q have been represented with transparency
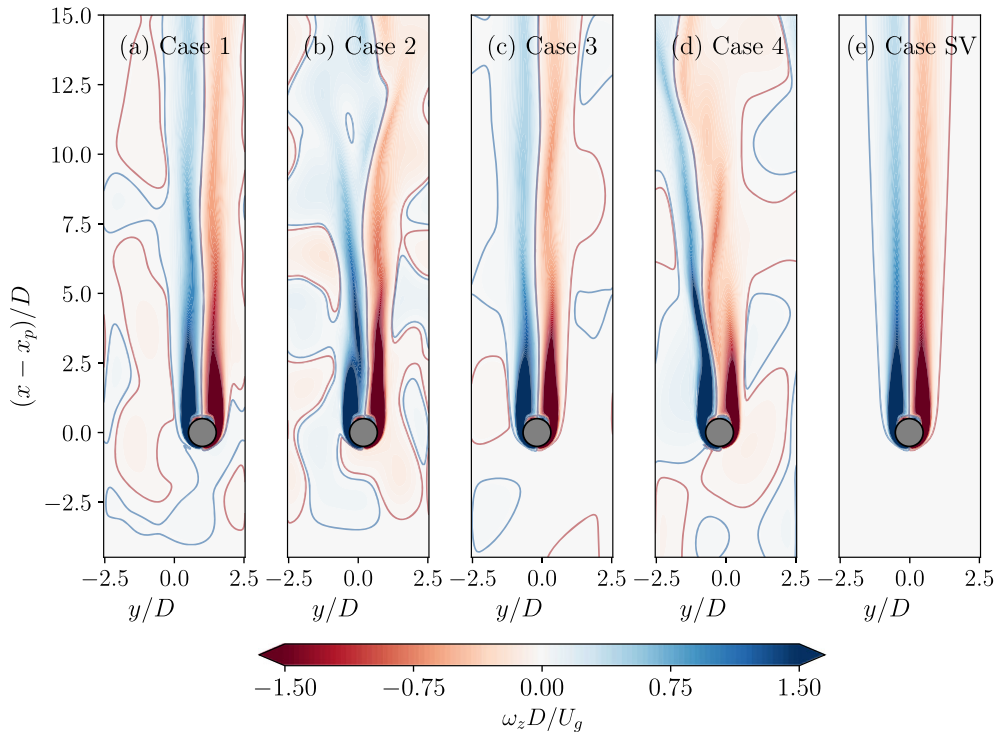
Fig. 3 Instantaneous flow fields at a plane passing through the center of the particle, for the nominal cases (1, 2, 3 and 4) and for the steady vertical case (SV, without ambient perturbations). The contours correspond to the vorticity perpendicular to the plane, ω_z. Red contour lines (——) represent small negative values of vorticity ($\omega_z D/U_g = -0.012$), whereas blue contour lines (——) represent small positive values of vorticity ($\omega_z D/U_g = 0.012$)

with the magnitude of the vorticity vector $\boldsymbol{\omega} = (\omega_x, \omega_y, \omega_z) = \nabla \times \mathbf{u}$. We use two thresholds for the isosurfaces of Q, namely $QD^2/U_g^2 = 1.2 \times 10^{-4}$ and 6×10^{-3}. In the absence of ambient perturbations, the only vortical structure present in the flow would be a toroidal vortex surrounding the particle , as seen in Fig. 2e. This toroidal vortex is also present in the perturbed flow for all cases, as shown in the figure. In addition, vortical structures with varying characteristics and intensities are readily identifiable over the whole domain. The two thresholds are employed to distinguish between structures that correspond to the ambient perturbations and fill the whole domain (isosurface with lower Q) and structures that are generated near the particle and remain in its vicinity or are shed into the wake (isosurface with higher Q). Although the second threshold is much bigger than the first threshold, its magnitude is still relatively small. This is due to the fact that although the toroidal vortex formed around the particle is intense, the double-threaded vortical structures shed into the wake are relatively weak, and require a small threshold to be visualized.

The effect of the size of the perturbations Λ can be explored by comparing Fig. 2a, b for $\Lambda = 1.137D$ with Fig. 2c, d for $\Lambda = 2.274D$. By looking also at the corresponding animations in the Supplementary Material, it is apparent that the flow for the cases 1 and 2 with smaller Λ seems to consist of less ordered flow structures. On the contrary, in the cases 3 and 4, it is observed a presence of threads of counter-rotating vorticity which are rather regularly shed in the wake of the particle. It is interesting to note that such vortical structures resemble those of the oscillating oblique regime found at a higher Galileo number [see for example [40], their figure 11]. In fact, the integral length of the perturbations of cases 3 and 4 ($\Lambda = 2.274D$) and the mean settling velocity of the particle U_s are such that the particle encounters the most energetic perturbations at a frequency of $f \simeq 0.08 U_g/D$, as we introduced in Sect. 2. This frequency roughly matches the vortex shedding frequency of the first unsteady mode ($f \simeq 0.07 U_g/D$, oblique oscillating mode) encountered when increasing the Galileo number. Note that the frequency of the first unsteady mode is almost constant for a wide range of density ratios (even light particles) as long as $\rho_p/\rho_f \lesssim 2$ [16]. For cases 1 and 2, the frequency of the perturbations that the particle encounters is twice as high. Therefore, a likely explanation to the present observations is that the ambient perturbations enhance or trigger the latent oscillating oblique mode. This occurs in a more efficient

way for cases 3 and 4 since the frequency that the particle encounters is nearly tuned to the frequency that corresponds to the path instability.

The effect of the intensity of the perturbations u' can be explored by comparing Fig. 2a, c for $u'/U_g = 1.23\%$ with Fig. 2b, d for $\Lambda = 3.7\%$, and the corresponding animations. The general impression is that more structures are visible when increasing the intensity of the perturbations. However, for both cases 3 and 4, the double-threaded quasi-streamwise vortices are consistently found, rather independently of the perturbation intensity. This also supports the idea that the larger perturbations are promoting the natural vortex shedding that would take place in quiescent ambient conditions at higher Ga.

Figure 3 shows 2D contours of the vorticity component normal to the plane. The figure shows the significantly higher vorticity levels in the vicinity of the particle (where the toroidal vortex is formed) compared to the vorticity levels corresponding to perturbations of the free stream. It can also be seen how the wake in the cases with less intense perturbations (cases 1 and 3, $u'/U_g = 1.23\%$) maintains a higher degree of alignment with the vertical direction compared with the cases with more intense perturbations (cases 2 and 4, $u'/U_g = 3.7\%$).
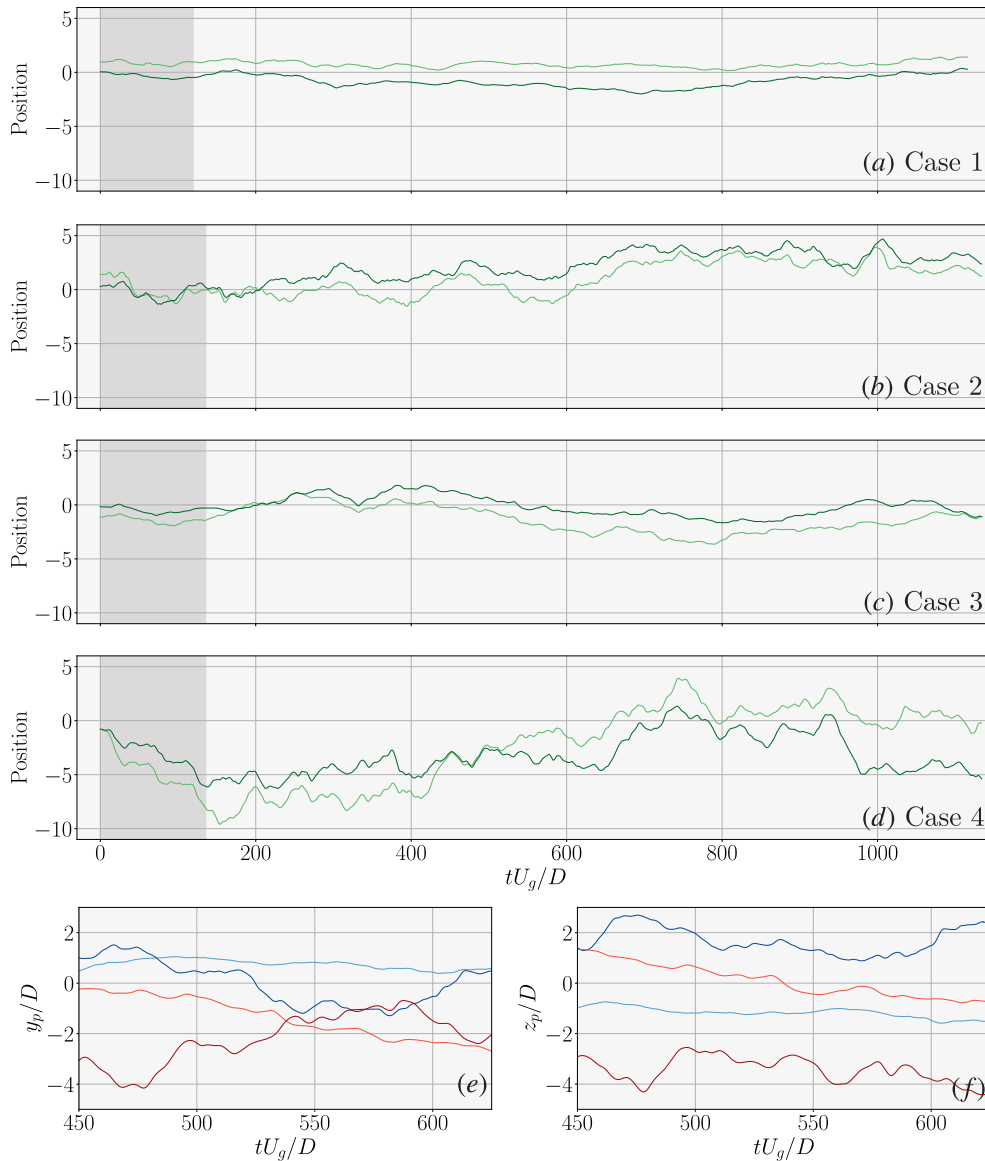

Fig. 4 **a**–**d** Temporal evolution of the horizontal position of the particle for each nominal case (y_p/D: ——, z_p/D: ——). The darker shaded region in **a**–**d** corresponds to the transient that has been discarded for the computation of statistics. **e**, **f** Contain a zoom in time for each horizontal component of the position (case 1: ——, case 2: ——, case 3: ——, case 4: ——)

The latter show a slightly tilted wake, especially further downstream of the particle, which can be attributed to the evolution of flow structures with a higher degree of unsteadiness. For the sake of comparison, Fig. 3e shows the case with no perturbations, where it can be seen that the setlling particle develops a steady axisymmetric wake, unlike the other cases.

4.2 Particle kinematics

We turn now our attention to the motion of the particle. As a result of the ambient perturbations, the particle is pushed randomly in all directions. This generates small oscillations with respect to the equilibrium position in the vertical direction and also lateral motion in the cross-plane. We focus in the following in the characterization of the lateral motion. Figure 4a–d shows the time history of the lateral position of the particle center for cases 1–4 (both y_p and z_p are shown). Please note that the vertical axis is longer than the lateral size of the computational domain. The axis has been extended using the periodicity of the domain to avoid jumps in the time history that are due to the particle leaving the domain from one side and entering from the opposite side.

The figure shows how the particle drifts along random directions during time intervals of variable duration. It is possible to see mild oscillations in the time signal, roughly on the time scale of the perturbations ($O(1)D/U_g$), that are more clearly visible in the zoom views provided in Fig. 4e, f. There are also prolonged motions on a much longer time scale, tens of times longer. The time histories of case 1 (smallest perturbations of lowest intensity, Fig. 4a) are reasonably smooth, with average lateral motions of about 2–3 D over a time interval of 1000 D/U_g. Increasing the intensity of the perturbations u', for the same length scale (case 2, Fig. 4b), results in longer drifts (overall $\sim 5D$) and a less smooth time evolution compared to case 1. When increasing the size of the perturbations, the lateral drifts are also increased: for example when comparing case 2 ($\Lambda = 1.137D$) and case 4 ($\Lambda = 2.274D$), both for the higher intensity, the drift increases from about 5 D to 10–12 D over the time interval considered.

Figure 4 therefore shows that both the size and the intensity of perturbations influence markedly the lateral trajectory of the particle. In order to characterize this influence, we define the horizontal particle velocity $u_{pH} = \sqrt{u_{py}^2 + u_{pz}^2}$, whose Probability Density Function (PDF) is shown in Fig. 5a. It can be seen that both increasing the intensity of the perturbations and their size contribute to shift the peak of the distribution to a higher value, with a tendency to broaden the distributions. Figure 5b–d shows the PDFs of u_{pH} normalized with the characteristic length of the perturbations, their intensity or a combination of both, respectively. It can
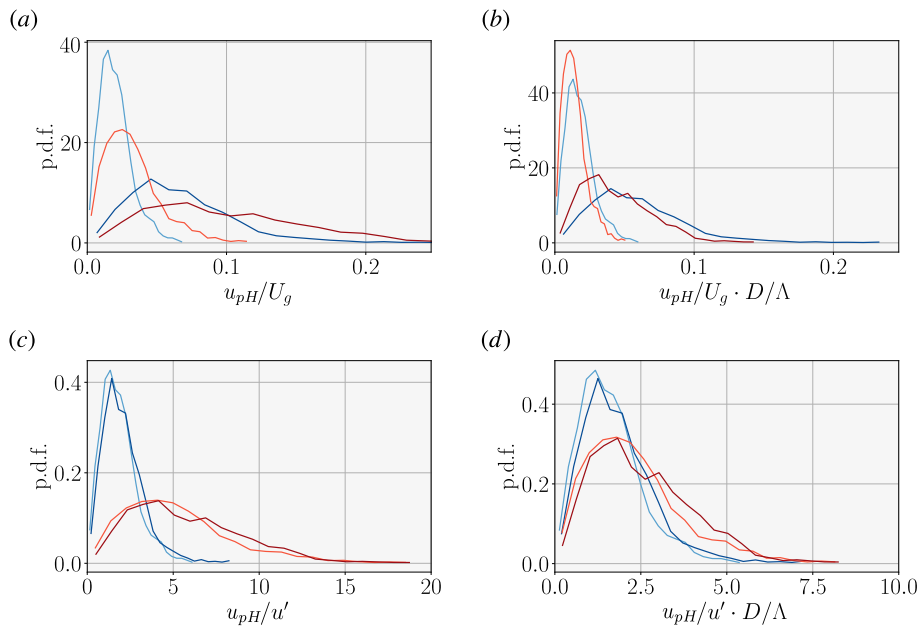

Fig. 5 Probablity density functions of the horizontal particle velocity u_{pH} normalized with different quantities (case 1: ——, case 2: ——, case 3: ——, case 4: ——)
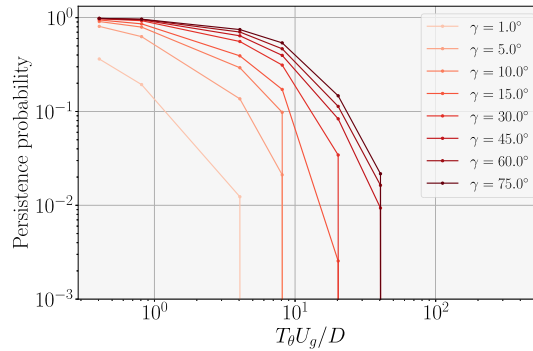
Fig. 6 Global probability of persistence of case 4 as a function of the characteristic time T_θ, for different values of the threshold angle γ

be seen that when the PDF is normalized with the intensity of the perturbations u', the curves of the cases whose perturbation intensity are the same almost collapse to a single curve (see Fig. 5c). On the other hand, when the reference quantity is the integral length of the perturbations Λ, the collapse of the PDF of cases is not so clear as it is with the intensity, but still satisfactory (see Fig. 5b). Finally, when combining both Λ and u' as the reference quantity, the peak of the four PDFs roughly matches but they do not completely collapse; the PDFs of the cases with larger fluctuations being somewhat broader than the other two. This suggests that the effect of the turbulent intensity on the cross-plane particle velocity is linear, while the effect of Λ is not.

4.3 Persistence

We have shown above that there are long time intervals in which the particle drifts slowly along a roughly fixed direction. For example, for case 3, there is a long drift from $t \sim 250D/U_{\rm g}$ to $790D/U_{\rm g}$, where the particle goes from $y_{\rm p} \sim 1D$ to $-3.5D$, without big deviations. This corresponds to lateral velocities $u_{py} \approx 0.008U_{\rm g}$, a velocity which is in the lower tail of the PDF, Fig. 5a. This indicates that the PDFs of the lateral velocity are useful to characterize the random motions of the particle but not the long-term drifts. In order to analyze the latter, we resort to the persistence (i.e., the probability that the particle moves along a fixed direction in the cross-plane), a concept introduced in Sect. 3.3. Since there are random motions superimposed on the slow drifts, we consider a tolerance γ within which we consider that the direction is fixed.

As an example, Fig. 6 shows, for case 4, the persistence probability as a function of the time interval, T_θ, for several values of γ. The figure shows how the persistence probability decreases monotonically when increasing the length of the time interval. This decay is rather abrupt when the tolerance is very small (corresponding to a strict definition of the fixed direction) but the decay is milder for intermediate values of the tolerance (such tolerance permits small, random excursions from the fixed direction). Therefore, it is now possible to use this information to compare the various cases. In order to do so, Fig. 7 shows the time interval T_θ during which the particle moves along a fixed direction as a function of the tolerance, γ, for specific values of the persistence probability, $P(T_\theta, \gamma) = 0.1$ and 0.75. It is apparent that the curves corresponding to larger-scale perturbations ($\Lambda = 2.274D$) are always above those of smaller-scale perturbations ($\Lambda = 1.137D$), indicating longer drifts on the former. Moreover, we note that there is not a significant difference between cases with the same perturbation size but different intensity, although the curves corresponding to higher intensity cases are generally above those of lower intensity, indicating that the intensity of the perturbations may not be a critical factor in determining the persistence of particle motion in the cross-plane direction. When the persistence probability is set to 10% ($P = 0.1$, Fig. 7a), we obtain reasonably long values of persistence time (about 10-20 $D/U_{\rm g}$ depending on γ). If we set a high value of the probability ($P = 0.75$, Fig. 7b), the resulting times are significantly lower and more in-line with the time scale of the perturbations that the particle encounters in each case.
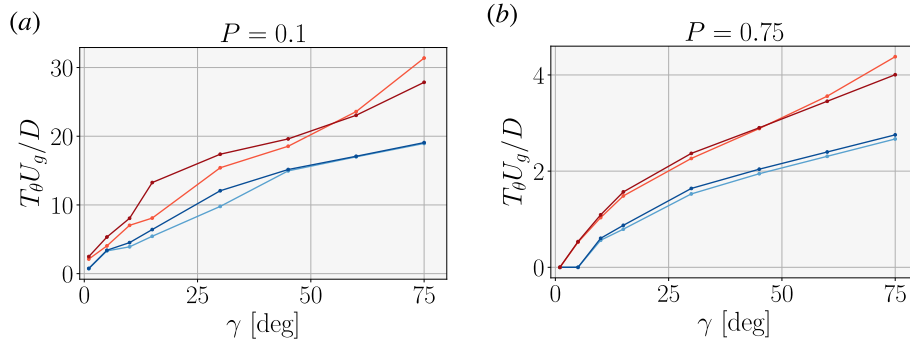
(a) $P = 0.1$
(b) $P = 0.75$

Fig. 7 Characteristic time T_θ in which the particle has a specific persistence probability, as a function of γ. Legend for figs. e,f): case 1 (——), case 2 (——), case 3 (——), case 4 (——)

4.4 Constrained dynamics

In order to assess the influence of rotation and vertical drifts on the overall motion of the particle, we also present three additional cases in which we have constrained the dynamics of the particle. These cases are listed in Table 2, where in cases 1.2 and 2.2, the particle is not permitted to move along the vertical direction, while in case 1.3, the rotation of the particle has been restricted.

Figure 8 includes the cases in which the particle motion is restricted in the vertical direction (cases 1.2 and 2.2), compared to the nominal cases with integral scale $\Lambda/D = 1.137$ (cases 1 and 2). Note that this configuration resembles those in which particles are towed in a perturbed flow (see Obligado and Bourgoin [28] as an example). Figure 8a depicts the PDF of these cases, whereas Fig. 8b shows the interval lengths that guarantee a given value of the persistence, as a function of the tolerance. Focusing on the cases where the particle is not moving along the x-direction, it is easy to see that there is little or almost no effect on the magnitude of the lateral velocity of the particle for the higher intensity case ($u'/U_g = 3.7\%$), while there is apparently a minor effect mainly on the peak of the PDF, for the lower intensity case ($u'/U_g = 1.23\%$), which is reduced with respect to the nominal case.

Similarly, Fig. 8b displays a very similar trend for all the cases shown, such that the difference in characteristic times is almost negligible among them, although it has to be remarked that the lines associated to the simulations with vertical motion restricted are almost always slightly above the ones moving freely. All in all, these observations suggest that restricting the particle motion in the vertical direction has a very limited effect, at times negligible, on the lateral motion of the particle.

Figure 9a displays the PDF of the lateral velocity magnitude, for the nominal case 1, together with case 1.3 that has the rotation of the particle restricted, showing that the differences in terms of lateral velocity magnitude are not very remarkable. Thus, for this problem, this essentially means that the rotation of the particle does not play a key role on the resultant particle velocity. On the other hand, we observe in Fig. 9b that the case with restricted particle rotation always exhibits lower persistence than the case with full particle rotation. This
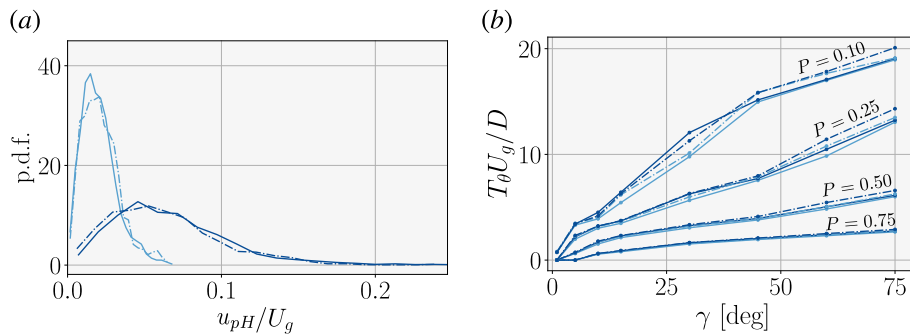

(a)
(b)

$P = 0.10$
$P = 0.25$
$P = 0.50$
$P = 0.75$

Fig. 8 a Probablity density functions of the cross-plane particle velocity u_{pH}, including the cases in which the particle motion is restricted in the vertical direction (cases 1.2 and 2.2). **b** Characteristic time T_θ in which the particle has an specific persistence probability, as a function of γ. Legend: case 1 (——), case 2 (——), case 1.2 (– · –), case 2.2 (– · –)

Table 2 Simulation parameters

Case	x_{stig}/D	Λ/D	u'/U_g	Rotation	Translation	Re$_s$
1	-4	1.137	1.23%	Enabled	XYZ	186.51
1.2	-4	1.137	1.23%	Enabled	YZ	186.56
1.3	-4	1.137	1.23%	Disabled	XYZ	186.61
2	-4	1.137	3.70%	Enabled	XYZ	186.52
2.2	-4	1.137	3.70%	Enabled	YZ	186

Please note that for cases 1.2 and 2.2, the particle does not move in the vertical direction X, hence its settling velocity is exactly equal to U_∞ and Re$_s$ is constant along the whole simulation
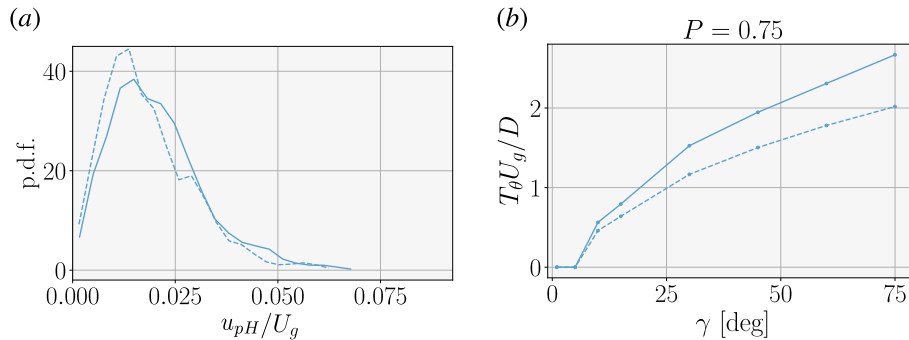
Fig. 9 **a** Probablity density functions of the cross-plane particle velocity u_{pH}, comparing case 1 with case 1.3 (rotation restricted). **b** Characteristic time T_θ in which the particle has an specific persistence probability, as a function of γ. Legend: case 1 (——), case 1.3 (- - -)

suggests that there is a non-negligible effect of the particle rotation on the persistence. One possible explanation for this is that restricting particle rotation inhibits the Magnus effect, which may be one of the mechanisms that enable particle motion to persist along specific directions.

5 Conclusions

We have performed direct numerical simulations of the settling of a spherical particle under the action of gravity in a slightly perturbed ambient fluid. The ambient perturbations were generated using the synthetic turbulence inflow generator method proposed by Schmidt and Breuer [34]. The Galileo number was chosen to be 151, while the solid-to-fluid density ratio was chosen to be $\varrho = 1.5$. With these parameters, in the absence of perturbations, the particle settles in a steady vertical trajectory. However, the selected Galileo number is close to the boundary in phase space that separates the steady vertical regime and the steady oblique regime. One aim of the study was to analyze if the presence of ambient perturbations triggers the transition to a neighboring flow regime. While no evidence has been found that the particle enters into the steady oblique regime in the presence of perturbations, a resemblance with the first unsteady flow regime (oblique oscillating) has been found. The ambient perturbations trigger the formation of threads of counter-rotating vorticity that are shed to the wake of the particle. These structures resemble those that appear in the oblique oscillating mode [40]. The effect is more clearly visible when the frequency of the encountered ambient perturbations is tuned to the frequency of the vortex shedding of the unsteady mode [16].

In addition, we have analyzed both qualitatively and quantitatively the particle response to the perturbations of different size and intensity. Due to the flow perturbations, the particle is pushed randomly in all directions, and this results in a combination of slow lateral drifts along fixed directions and relatively fast excursions in random directions. The statistical characterization of the particle motion has required therefore very long integration times (more than 1000 non-dimensional time units). It has been found that the probability density functions of the velocity in the cross-plane tend to broaden when the size and/or intensity of the fluctuations is increased. However, when properly re-scaled using both the size and the intensity of the fluctuations, the peak of the PDFs collapses reasonably well.

Finally, in order to characterize the slow particle drifts, we have performed a persistence analysis. We have found that the drifts are influenced by the size of the perturbations, while the intensity of the perturbations seems

to play a minor role. The drifts become more apparent as the characteristic length of the ambient perturbations become larger, but they are attenuated as the rotation of the particle is restricted, suggesting that the Magnus effect is playing a relevant role in the process.

A Generation of perturbation velocity using digital filters

In order to generate the perturbation velocity field $\mathbf{u}'_f(t, y, z)$, the digital filtering approach of Kempf et al. [19] is used. The process consists of filtering a set of random numbers $r_\alpha(i', j, k)$, for $\alpha = [x, y, z]$, as follows:

$$h_{1\alpha}(j, k) = \sum_{i'=-N_x}^{N_x} b_x(i') \cdot r_\alpha(i', j, k), \tag{8a}$$

$$h_{2\alpha}(j, k) = \sum_{j'=-N_y}^{N_y} b_y(j') \cdot h_{1\alpha}(j + j', k), \tag{8b}$$

$$u'_{f,\alpha}(j, k) = \sum_{k'=-N_z}^{N_z} b_z(k') \cdot h_{2\alpha}(j, k + k'), \tag{8c}$$

where (j, k) are the indices of the nodes in the STIG injection plane, (N_x, N_y, N_z) are the filter support half-size per direction, (i', j', k') are the indices within the filter support, and (b_x, b_y, b_z) are the filter coefficients, defined below. Some intermediate buffers, $h_{1\alpha}$ and $h_{2\alpha}$, are created along the filtering process. These buffers contain the information of the filtered random numbers at intermediate steps. As shown, the filter operation is performed progressively by axis, first along x (8a) (which will be analogous to time), then along y (8b) and finally along z (8c). These operations are done for each velocity component.

In Eq. (8), the indices (j, k) are defined in the intervals $j \in [1, M_y]$ and $k \in [1, M_z]$, with M_y, M_z the number of nodes in y and z directions, respectively ($M_y \times M_z$ denotes the dimensions of the computational grid in the inflow plane). The indices (i', j', k') are the indices going over the filter support, i.e., $i' \in [-N_x, N_x]$, $j' \in [-N_y, N_y]$, $k' \in [-N_z, N_z]$. As explained below, the filter support is related to the time and length scales of the perturbation velocity field, $\mathbf{u}'_f(t, y, z)$. The periodicity of the perturbation velocity field requires the buffers r_α, $h_{1\alpha}$ and $h2_\alpha$ to be periodic in the j- and k-directions, which is accounted for in the implementation of (8) in our solver.

As in Klein et al. [20], we use Gaussian filters to impose the correlation length of the velocity perturbations. The filter coefficients b_β, for $\beta = [x, y, z]$, are computed as

$$b_\beta(k) \approx \tilde{b}_\beta(k) \left/ \left(\sum_{j=-N_\beta}^{N_\beta} \tilde{b}_\beta^2(j) \right)^{1/2} \right. \quad \text{with} \quad \tilde{b}_\beta(k) = \exp\left(-\frac{\pi k^2}{2n_\beta^2} \right), \tag{9}$$

with n_β being the number of points per length scale $n_\beta = \Lambda/\Delta\beta$, the filter support $N_\beta \geq 2n_\beta$ and $k \in [-N_\beta, N_\beta]$. To enforce that the integral length scale of the generated velocity perturbations is equal to the input length scale Λ, we choose the number of points per length scale and the corresponding filter supports as:

$$n_x = T/\Delta t \equiv \Lambda/(U_\infty \Delta t), \qquad N_x = 2n_x \tag{10a}$$

Table 3 Simulation parameters and values of the intensity u'/U_g, nominal and at different locations ($x/D = [-2, 0, 2]$)

Case	x_stig/D	Λ/D	u'/U_g (%)	u'_{-2}/U_g (%)	u'_0/U_g (%)	u'_2/U_g (%)
1	-4	1.137	1.23	1.17	1.11	1.05
2	-4	1.137	3.70	3.21	3.08	2.84
3	-6.5	2.274	1.23	1.17	0.69	0.64
4	-6.5	2.274	3.70	1.97	1.85	1.73

$$n_y = \Lambda/\Delta y, \quad N_y = 2n_y \tag{10b}$$

$$n_z = \Lambda/\Delta z, \quad N_z = 2n_z. \tag{10c}$$

We use Taylor's Hypothesis [36] to relate the time scale T and the length scale in the streamwise direction Λ, so that $T = \Lambda/U_\infty$, where U_∞ is the free-stream velocity. This yields a velocity perturbation field downstream of the injection plane where all velocity components have the same correlation length in all directions, as expected in an isotropic velocity field. Note also that this requires a sequential update of r_α in time, a procedure that is described in detail in [20].

Following the above procedure, we generate flow perturbations of roughly the desired intensity in the vicinity of the injection plane. The perturbations slowly decay along the streamwise direction, and the intensity that the particle experiences is somewhat lower. The decay is quantified in Table 3 that presents the values of the intensity of the fluctuations measured at different locations, to provide a reference of the range that the particle is actually experimenting.

References

1. Arranz, G., Moriche, M., Uhlmann, M., Flores, O., García-Villalba, M.: Kinematics and dynamics of the auto-rotation of a model winged seed. Bioinspiration Biomim. **13**(3), 036011 (2018)
2. Balachandar, S., Eaton, J.K.: Turbulent dispersed multiphase flow. Annu. Rev. Fluid Mech. **42**, 111–133 (2010)
3. Bercin, K.M., Xie, Z.-T., Turnock, S.R.: Exploration of digital-filter and forward-stepwise synthetic turbulence generators and an improvement for their skewness-kurtosis. Comput. Fluids **172**, 443–466 (2018)
4. Brandt, L., Coletti, F.: Particle-laden turbulence: progress and perspectives. Annu. Rev. Fluid Mech. **54**, 159–189 (2022)
5. Bray, A.J., Majumdar, S.N., Schehr, G.: Persistence and first-passage properties in nonequilibrium systems. Adv. Phys. **62**(3), 225–361 (2013)
6. Breuer, M.: Effect of inflow turbulence on an airfoil flow with laminar separation bubble: an LES study. Flow Turbul. Combust. **101**(2), 433–456 (2018)
7. Cabrera-Booman, F., Plihon, N., Bourgoin, M.: Path instabilities and drag in the settling of single spheres. arxiv preprint arXiv:2304.11147 (2023)
8. Catalán, J.M., Olivieri, S., Garcia-Villalba, M., Flores, O.: On the generation of free-stream turbulence at low Reynolds number: a numerical study (submitted) (2023)
9. De Nayer, G., Schmidt, S., Wood, J.N., Breuer, M.: Enhanced injection method for synthetically generated turbulence within the flow domain of eddy-resolving simulations. Comput. Math. Appl. **75**(7), 2338–2355 (2018)
10. Ern, P., Risso, F., Fabre, D., Magnaudet, J.: Wake-induced oscillatory paths of bodies freely rising or falling in fluids. Annu. Rev. Fluid Mech. **44**, 97–121 (2012)
11. Fornari, W., Ardekani, M.N., Brandt, L.: Clustering and increased settling speed of oblate particles at finite Reynolds number. J. Fluid Mech. **848**, 696–721 (2018)
12. Horowitz, M., Williamson, C.H.K.: The effect of Reynolds number on the dynamics and wakes of freely rising and falling spheres. J. Fluid Mech. **651**, 251–294 (2010)
13. Huisman, S.G., Barois, T., Bourgoin, M., Chouippe, A., Doychev, T., Huck, P., Bello Morales, C.E., Uhlmann, M., Volk, R.: Columnar structure formation of a dilute suspension of settling spherical particles in a quiescent fluid. Phys. Rev. Fluids **1**(7), 074204 (2016)
14. Hunt, J.C.R. , Wray, A.A., Moin, P.: Eddies, streams, and convergence zones in turbulent flows. Studying turbulence using numerical simulation databases, 2. In: Proceedings of the 1988 Summer Program (1988)
15. Jarrin, N., Benhamadouche, S., Laurence, D., Prosser, R.: A synthetic-eddy-method for generating inflow conditions for large-eddy simulations. Int. J. Heat Fluid Flow **27**(4), 585–593 (2006)
16. Jenny, M., Dušek, J., Bouchet, G.: Instabilities and transition of a sphere falling or ascending freely in a Newtonian fluid. J. Fluid Mech. **508**, 201–239 (2004)
17. Juneja, A., Lathrop, D.P., Sreenivasan, K.R., Stolovitzky, G.: Synthetic turbulence. Phys. Rev. E **49**(6), 5179 (1994)
18. Kempf, A., Klein, M., Janicka, J.: Efficient generation of initial-and inflow-conditions for transient turbulent flows in arbitrary geometries. Flow Turbul. Combust. **74**(1), 67–84 (2005)
19. Kempf, A.M., Wysocki, S., Pettit, M.: An efficient, parallel low-storage implementation of Klein's turbulence generator for LES and DNS. Comput. Fluids **60**, 58–60 (2012)
20. Klein, M., Sadiki, A., Janicka, J.: A digital filter based generation of inflow data for spatially developing direct numerical or large eddy simulations. J. Comput. Phys. **186**(2), 652–665 (2003)

21. Lund, T.S., Wu, X., Squires, K.D.: Generation of turbulent inflow data for spatially-developing boundary layer simulations. J. Comput. Phys. **140**(2), 233–258 (1998)
22. Mittal, R.: Response of the sphere wake to freestream fluctuations. Theor. Comput. Fluid Dyn. **13**(6), 397–419 (2000)
23. Moriche, M.: A Numerical Study on the Aerodynamic Forces and the Wake Stability of Flapping Flight at Low Reynolds Number. Ph.D. thesis, Universidad Carlos III de Madrid (2017)
24. Moriche, M., Flores, O., García-Villalba, M.: On the aerodynamic forces on heaving and pitching airfoils at low Reynolds number. J. Fluid Mech. **828**, 395–423 (2017)
25. Moriche, M., Uhlmann, M., Dušek, J.: A single oblate spheroid settling in unbounded ambient fluid: a benchmark for simulations in steady and unsteady wake regimes. Int. J. Multiph. Flow **136**, 103519 (2021)
26. Moriche, M., Hettmann, D., García-Villalba, M., Uhlmann, M.: On the clustering of low-aspect-ratio oblate spheroids settling in ambient fluid. J. Fluid Mech. **963**, A1 (2023)
27. Natarajan, R., Acrivos, A.: The instability of the steady flow past spheres and disks. J. Fluid Mech. **254**, 323–344 (1993)
28. Obligado, M., Bourgoin, M.: Dynamics of towed particles in a turbulent flow. J. Fluids Struct. **114**, 103704 (2022)
29. Pamiès, M., Weiss, P.-E., Garnier, E., Deck, S., Sagaut, P.: Generation of synthetic turbulent inflow data for large eddy simulation of spatially evolving wall-bounded flows. Phys. Fluids **21**(4), 045103 (2009)
30. Roidl, B., Meinke, M., Schröder, W.: A reformulated synthetic turbulence generation method for a zonal RANS-LES method and its application to zero-pressure gradient boundary layers. Int. J. Heat Fluid Flow **44**, 28–40 (2013)
31. Salcedo-Sanz, S., Casillas-Pérez, D., Del Ser, J., Casanova-Mateo, C., Cuadra, L., Piles, M., Camps-Valls, G.: Persistence in complex systems. Phys. Rep. **957**, 1–73 (2022)
32. Schiller, L., Naumann, A.Z.: A drag coefficient correlation. Ver. Deut. Ing. **77**, 318–320 (1933)
33. Schmidt, S., Breuer, M.: Extended synthetic turbulence inflow generator within a hybrid LES-URANS methodology for the prediction of non-equilibrium wall-bounded flows. Flow Turbul. Combust. **95**, 669–707 (2015)
34. Schmidt, S., Breuer, M.: Source term based synthetic turbulence inflow generator for eddy-resolving predictions of an airfoil flow including a laminar separation bubble. Comput. Fluids **146**, 1–22 (2017)
35. Subramaniam, S., Balachandar, S.: Modeling Approaches and Computational Methods for Particle-Laden Turbulent Flows. Academic Press, Cambridge (2022)
36. Taylor, G.: The spectrum of turbulence. Proc. R. Soc. Lond. A Math. Phys. Sci. **164**(919), 476–490 (1938)
37. Tomboulides, A.G., Orszag, S.A.: Numerical investigation of transitional and weak turbulent flow past a sphere. J. Fluid Mech. **416**, 45–73 (2000)
38. Uhlmann, M.: An immersed boundary method with direct forcing for the simulation of particulate flows. J. Comput. Phys. **209**(2), 448–476 (2005)
39. Uhlmann, M., Doychev, T.: Sedimentation of a dilute suspension of rigid spheres at intermediate Galileo numbers: the effect of clustering upon the particle motion. J. Fluid Mech. **752**, 310–348 (2014)
40. Uhlmann, M., Dušek, J.: The motion of a single heavy sphere in ambient fluid: a benchmark for interface-resolved particulate flow simulations with significant relative velocities. Int. J. Multiph. Flow **59**, 221–243 (2014)
41. Wu, X.: Inflow turbulence generation methods. Annu. Rev. Fluid Mech. **49**, 23–49 (2017)
42. Xie, Z.-T., Castro, I.P.: Efficient generation of inflow conditions for large-eddy simulation of street-scale flows. Flow Turbul. Combust. **81**(3), 449–470 (2008)
43. Yin, X., Koch, D.L.: Hindered settling velocity and microstructure in suspensions of solid spheres with moderate Reynolds numbers. Phys. Fluids **19**(9), 093302 (2007)
44. Zhou, W., Dušek, J.: Chaotic states and order in the chaos of the paths of freely falling and ascending spheres. Int. J. Multiph. Flow **75**, 205–223 (2015)